PAPER

Check for updates

Unravelling the amplified spontaneous emission mechanism in three-dimensional metal halide perovskites

Gayoung Lee,†[a] Jinhong Kim,†[b,c] EunSeo Jang, [b] Hyeonji Lee,[a,d] Yejin Jun,[a,d] Minhyuk Lee,[b] JunWoo Kim [b] *[b,c] and Kwangdong Roh [b] *[a,d]

Metal halide perovskites have demonstrated outstanding optical gain properties, attracting extensive research for their potential in laser applications. To further improve their lasing performance, a detailed understanding of underlying light amplification is essential. Herein, we investigate how film thickness influences amplified spontaneous emission (ASE) properties in the methylammonium lead iodide (MAPbI₃) perovskite. By carefully maintaining consistent material composition and crystallinity, we isolate the effect of film thickness on ASE behavior. Femtosecond pump–probe spectroscopy reveals that thinner films facilitate the formation of multiexciton (ME) states, which are strongly correlated with ASE transitions. However, thin films suffer from weaker optical confinement, limiting photon feedback. In contrast, thicker films exhibit enhanced optical confinement but reduced ME population. The influences of thickness-dependent exciton-state dynamics and optical confinement explain the non-monotonic variation in the ASE threshold, which reaches its lowest value near 150 nm, where exciton generation and optical confinement are optimally balanced to maximize light amplification. These findings offer practical design guidelines for the development of high-performance perovskite laser devices.

Introduction

Lasers play a critical role across a broad range of applications, including communications, sensing, biomedical imaging, and quantum information processing.[1–3] Among emerging candidates for next-generation coherent light sources, metal halide perovskites are considered highly promising due to their large stimulated emission cross-sections, high photoluminescence quantum yields, and bandgap tunability with low-cost processing.[4–6] Lasing under optical pumping has been reported under diverse conditions – from pulsed to continuous-wave operation – enabled by various feedback structures such as distributed feedback gratings, Fabry–Pérot cavities, and whispering gallery modes.[7–14] In addition, the ability to deposit high-quality thin films on a wide range of substrates through solution-based methods makes perovskites attractive

for integrated photonics.[15] Nonetheless, electrically pumped lasing has not yet been demonstrated due to the difficulty of achieving sufficiently low lasing or amplified spontaneous emission (ASE) thresholds under electrical injection.[15,16]

To address this issue, many studies have focused on reducing the ASE threshold through improvements in the composition of perovskite materials. Strategies such as dimensional confinement (e.g., quasi-2D based on the Ruddlesden–Popper or Dion–Jacobson phase), compositional engineering, defect passivation, and interfacial modification have been employed to enhance radiative efficiency and minimize non-radiative recombination.[17–20] While these approaches have led to meaningful progress in optical gain performance, the design of optical structures that support optimal light amplification – particularly the influence of film thickness, optical confinement, and carrier generation profiles – has been less extensively explored. Thickness-dependent ASE behavior has been investigated in organic semiconductors, primarily involving low-absorbing gain materials with emission in the blue or green spectral regions.[21,22] In contrast, metal halide perovskites such as methylammonium lead iodide (MAPbI₃) exhibit much stronger absorption and emit in the near-infrared region, resulting in distinct thickness-dependent ASE characteristics. Although thickness-dependent ASE in halide perovskites has been reported,[23–25] studies that cover a broad thickness range (up to ~450 nm) and account for all higher-order

[a] Department of Physics, Ewha Womans University, Seoul 03760, Republic of Korea. E-mail: kroh@ewha.ac.kr
[b] Department of Chemistry, Chungbuk National University, Cheongju 28644, Republic of Korea. E-mail: jwkim0@cbnu.ac.kr
[c] Advanced Basic Science and Convergence Institute, Chungbuk National University, Cheongju 28644, Republic of Korea
[d] Institute for Multiscale Matter and Systems, Ewha Womans University, Seoul 03760, Republic of Korea
† These authors contributed equally to this work.

guided modes remain limited. Previous studies employing femtosecond time-resolved spectroscopy have investigated carrier dynamics related to ASE in various perovskite systems.[26–28] Nonetheless, the specific electronic transitions responsible for ASE in MAPbI$_3$ – particularly multiexciton–single exciton (ME–SE) transitions – and their dependence on photonic geometry remain insufficiently explored.

In perovskite solar cells, film thickness is a significant factor in balancing optical absorption and carrier transport. Although metal halide perovskites such as MAPbI$_3$ exhibit high absorption coefficients,[29] complete absorption of the solar spectrum requires absorber layers on the order of several hundred nanometers. Empirically, a thickness of approximately 400–600 nm ensures efficient photon absorption across the visible and near-infrared range. Importantly, this thickness range is also compatible with the relatively long carrier diffusion lengths observed in high-quality perovskite films, often exceeding 1 μm,[30] which enables photogenerated carriers to reach the electrodes without significant recombination losses. Moreover, thicker films are less susceptible to interfacial recombination and are better able to suppress morphological defects, such as pinholes, contributing to improved device stability.[31] These considerations have led to the widespread adoption of ~500 nm thick perovskite layers in high-efficiency photovoltaic architectures.

In perovskite light-emitting diodes (LEDs), however, ultrathin active layers – often below 50 nm – are employed to enhance radiative recombination efficiency.[32–34] These thin films confine the electron–hole recombination zone within a narrow spatial region, thereby minimizing exciton quenching at the interfaces with charge transport layers and reducing carrier leakage.[35,36] From a thermal perspective, reduced thickness mitigates Joule heating and suppresses thermal quenching under continuous operation, both of which are detrimental to emission efficiency.[37–39] Additionally, thin perovskite layers facilitate favorable optical interference, improving the light-outcoupling efficiency.[34,40] Taken together, these factors have established thin perovskite layers as a critical design choice for achieving high-performance LED operation.

In this study, we investigate how the film thickness of perovskites influences the ASE threshold to determine the optimal thickness regime for efficient light amplification. Rather than focusing on compositional or dimensional variations, we selected MAPbI$_3$ – one of the most extensively studied perovskite systems – as a target material to isolate the effect of film thickness. By systematically varying the thickness while maintaining consistent crystallinity and optical quality, we analyze the thickness dependence of ASE behavior across a broad thickness range. ASE characterization studies, based on steady-state and femtosecond pump–probe (PP) spectroscopy, show a non-monotonic dependence on film thickness, with a clear minimum near 150 nm where optical confinement and carrier generation are optimally balanced. These findings highlight the importance of photonic geometry in gain properties and provide quantitative design guidelines for optimizing perovskite laser structures beyond materials-centric optimization strategies.

Results and discussion

To investigate light amplification in perovskite thin films, we constructed the experimental setup shown in Fig. 1a. A
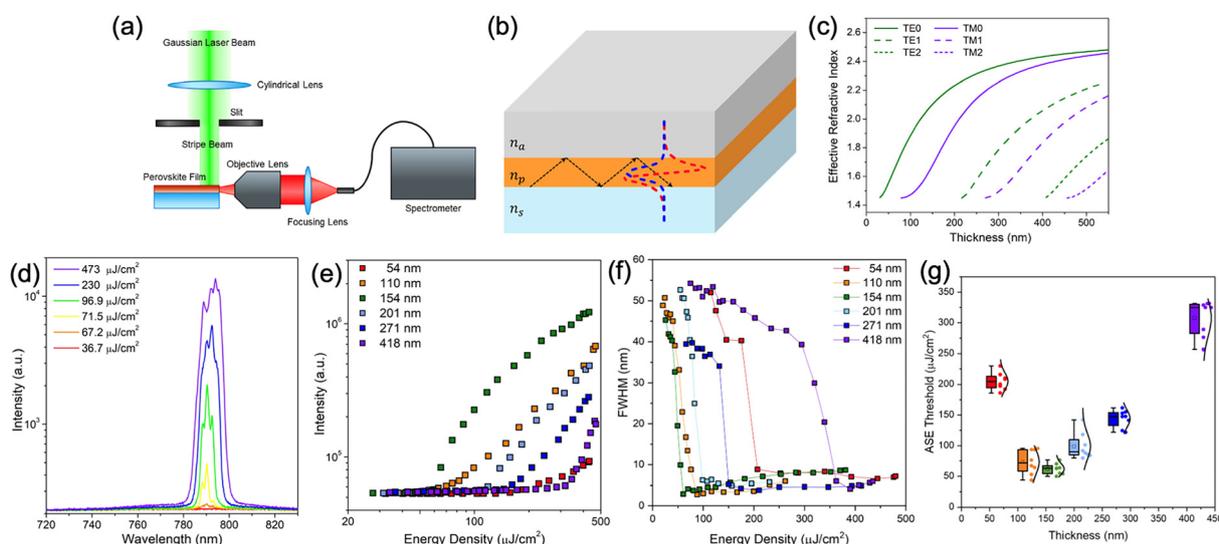

Fig. 1 (a) Schematic illustration of the experimental setup for ASE measurements using a stripe excitation and edge-collection geometry. (b) Cross-sectional illustration of the slab-waveguide structure of a perovskite thin film sandwiched between air and a glass substrate. (c) Calculated effective refractive indices of the guided TE and TM modes as a function of film thickness, indicating cutoff conditions for higher-order modes. (d) Representative emission spectra obtained under various excitation fluences for a 154 nm thick film, showing the onset of ASE. (e) Input−output curves for perovskite films of varying thicknesses, showing distinct threshold behaviors. (f) FWHM curves for perovskite films of varying thicknesses. (g) Extracted ASE threshold fluence as a function of film thickness.

Gaussian laser beam was expanded and then shaped into the geometry of a stripe using a cylindrical lens. A central portion of the beam with relatively uniform intensity was selected by a slit and used for excitation (over an area of approximately 500 μm × 30 μm). Upon excitation of the perovskite film with the stripe-shaped beam, the emitted photons were collected from the cleaved edge of the sample and analyzed using a fiber-coupled spectrometer. In a perovskite film, ASE is generated when spontaneously emitted photons are amplified through stimulated emission as they propagate within the gain medium. Here, the gain must be sufficient to overcome the optical losses, and the emitted photons must be confined and travel sufficient distance within the gain region to undergo amplification.[41,42] This situation can be modeled as a slab waveguide structure, as shown in Fig. 1b. Due to the relatively high refractive index of the perovskite layer, n_p (typically ~2.55 for the MAPbI$_3$ perovskite at an emission wavelength of ~790 nm, based on our previously reported ellipsometry measurement for the same material system[42]) compared to that of the substrate (n_s) and air (n_a), light can be confined via total internal reflection at the layer boundaries. However, guided modes are only supported when the film thickness exceeds a certain threshold, known as the cutoff thickness. If the perovskite layer is thinner than this, in-plane confinement is not supported, and the photons leak out of the waveguide before being amplified.

Fig. 1c shows the calculated effective refractive indices as a function of perovskite film thickness at a wavelength of $λ$ = 790 nm, corresponding to the ASE emission peak of MAPbI$_3$ films. The cutoff thickness for the fundamental transverse electric (TE) mode is estimated to be approximately 30 nm. Consistent with this analysis, ASE was not observed in films thinner than 50 nm. For MAPbI$_3$ perovskite films in the 30–80 nm thickness range, only a single TE$_0$ mode is predicted to be supported based on this slab-waveguide calculation, while thicker films support multiple guided modes. As shown in Fig. S1a and S1b, ASE from a 75 nm thick film is exclusively TE-polarized, confirming the presence of only the TE$_0$ mode. In contrast, the emission from a 200 nm thick film exhibits both TE and transverse magnetic (TM) polarizations, as evidenced by the spectral curves in Fig. S1c and S1d.

Fig. 1d shows the representative photoluminescence spectra of a MAPbI$_3$ perovskite thin film with a thickness of 154 nm under varying excitation fluences. At low excitation levels, only the spontaneous emission spectrum is observed, characterized by broad spectral linewidths centered around 775 nm. As the excitation fluence increases beyond 67.2 μJ cm^{-2}, a spectrally narrowed band emerges within the 780–800 nm range, indicating the onset of ASE. Within this band, several sharp spectral spikes appear, which are attributed to randomly formed resonant modes supported by scattering centers such as microcrystalline grain boundaries and nano-crystalline domains in the polycrystalline film.[43] Further increases in excitation fluence result in a dramatic increase in emission intensity, with the output predominantly concentrated within the optical gain bandwidth.

To systematically investigate the influence of film thickness on ASE characteristics, a series of MAPbI$_3$ perovskite films with identical composition but varying thicknesses were prepared. The film thickness was controlled by tuning the precursor solution concentration from 0.2 M to 1.2 M, yielding films ranging from 54 nm to 418 nm in thickness. Each film thickness was determined from multiple profilometer measurements taken at several positions across the central region of the sample, and the final value was obtained by averaging after excluding the highest and lowest readings (see Fig. S2). X-ray diffraction analysis confirmed that all films, despite their differing thicknesses, shared the same crystal structure (Fig. S3). Furthermore, atomic force microscopy (AFM) and scanning electron microscopy (SEM) measurements (Fig. S4 and S5) verify that the surface roughness and grain morphology remain essentially unchanged across the different film thicknesses. The root-mean-square roughness values extracted from 2 μm × 2 μm AFM scans fall within a narrow range (6.01–7.76 nm), and the SEM images consistently show similar grain size and morphology. This ensures that variations in optical properties arising from the morphology are negligible, validating our assumption that the observed differences in ASE behavior can be attributed primarily to the change in film thickness, thereby isolating thickness as the sole variable influencing ASE behavior.

To further verify that other loss mechanisms do not change significantly with film thickness, we also measured the optical propagation loss using the shifting-excitation-spot (SES) method. In this technique, the excitation spot is gradually moved away from the collection edge, and the decay of the guided emission intensity is used to extract the effective loss coefficient. SES measurements performed on the films with several different thicknesses yielded nearly identical loss values in the range of 86–90 cm^{-1} (Fig. S6), indicating that nonradiative recombination, scattering, and parasitic absorption do not exhibit meaningful thickness-dependent variation. Fig. 1e displays the input–output characteristics for the films of various thicknesses. To determine the threshold, the emission intensity was obtained by integrating the ASE band within a fixed ~15 nm spectral window centered on the gain peak, rather than relying on a single spectral spike, thus avoiding ambiguities introduced by the multi-peak structure in the ASE spectra. The corresponding full width at half maximum (FWHM) evolution shown in Fig. 1f exhibits a sharp linewidth collapse at the ASE onset, consistent with the threshold fluences extracted from the input–output curves. A clear threshold behavior is observed for all samples, where both the ASE threshold fluence and the maximum output intensity strongly depend on the film thickness. The corresponding ASE threshold fluences, extracted from the curves, are summarized in Fig. 1g. A clear non-monotonic trend emerges: the lowest ASE threshold occurs at a film thickness of 154 nm, while both thinner and thicker films exhibit significantly higher thresholds.

The higher value of ASE thresholds observed in the thinner films can be attributed to insufficient optical confinement near the cutoff waveguiding. Notably, no ASE was detected in

films thinner than 50 nm, which is attributed to the lack of guided modes below the cutoff thickness. As shown in Fig. 1c, the effective refractive index for such thin perovskite layers remains below ~1.5 – comparable to that of the underlying glass substrate – which significantly weakens the lateral optical confinement. This suggests that, despite sufficient material gain, the lack of guided-mode feedback in this regime prevents the onset of ASE, thereby requiring much higher excitation fluence to achieve population inversion over an effectively lossy propagation path.

To gain deeper insight into the ASE mechanism of perovskite films, it is essential to selectively analyze the excited-state dynamics that are directly associated with the optical gain. This can be achieved by comparing the transient responses under sufficient excitation fluence conditions where the ASE band is observed with those where it is absent. To this end, we performed femtosecond PP spectroscopy under both ASE and non-ASE conditions to isolate the dynamics relevant to population inversion. The PP technique measures the time-dependent changes in the transition properties of a material induced by an optical pump pulse.[44,45] In the experiment, a femtosecond pulse with a carrier wavelength of 480 nm was used as the pump, and a broadband white-light continuum served as the probe (Fig. 2a). The temporal resolution of the measurement was approximately 100 fs.

Fig. 2b presents the femtosecond-resolved PP spectra of a 154 nm thick perovskite film under three different excitation fluences. Regardless of the excitation power, a pronounced photoinduced bleach (PIB) band emerges consistently near

750 nm.[44] Upon increasing the pump fluence, a photoinduced absorption (PIA) band rapidly increases around time zero at 770 nm, indicating the presence of higher-lying excited states. The strong PIA band observed under high pump fluence is likely associated with the ME states, as suggested by its power dependence and peak position.[46,47] However, due to the spectral overlap with the dominant PIB peak, extracting clear kinetic information from this region remains challenging. Additionally, a narrow emission band appearing near 780 nm is identified as the ASE band generated by intense photoexcitation. The weak time-independent signal observed around the ASE band is attributed to spontaneous emission from the sample. It is important to note that since this ASE is generated solely by the pump pulse, it does not exhibit dependence on the pump–probe time delay and thus appears as a time-independent feature in the PP spectra. The emergence of the ASE band provides a more distinct signature of the net optical gain condition, allowing the transient spectral response to be categorized into ASE and non-ASE regimes based on its presence.

Fig. 2c displays the PP spectra of perovskite films with two different thicknesses (54 nm and 418 nm) under varying excitation fluences in a picosecond window. (See Fig. S7 and S8 for the PP spectra obtained across a broader range of film thicknesses, and Fig. S9 for the transient spectra obtained at selected delay times.) Notably, the thinner film exhibits a stronger dependence on excitation power, as evidenced by distinct changes in transient responses. Two characteristic features emerge under high excitation power: (i) a broad PIB band appears on the blue side of the dominant PIB signal and
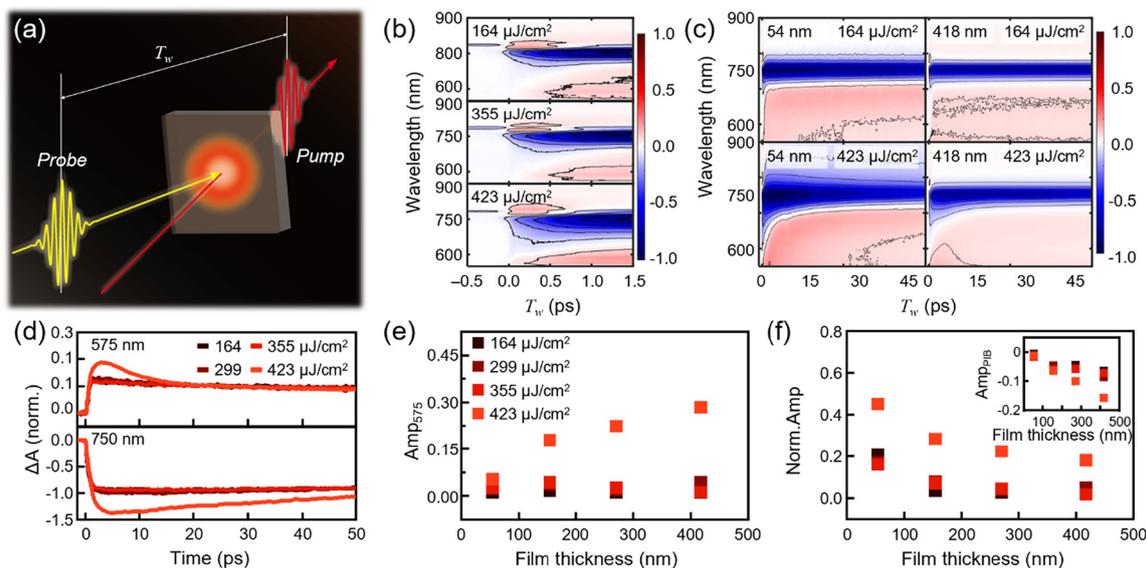

Fig. 2 (a) Schematic illustration of the femtosecond PP spectroscopy setup applied to perovskite thin films. (b) Transient absorption maps of a 154 nm thick perovskite film measured at pump fluences of 164 μJ cm^{-2} (top), 355 μJ cm^{-2} (middle) and 423 μJ cm^{-2} (bottom) within a femtosecond time window. (c) Transient absorption spectra of 54 nm thick (left) and 418 nm thick (right) perovskite films under pump fluences of 164 μJ cm^{-2} (top) and 423 μJ cm^{-2} (bottom) on a picosecond time scale. (d) Normalized transient kinetics at 575 and 750 nm for the 54 nm thick film, highlighting excitation power-dependent spectral dynamics. (e) Amplitude of the 15 ps component (Amp$_{575}$) as a function of thickness and pump fluence. (f) Normalized amplitude (Amp$_{575}$/Amp$_{750}$) showing the relative contribution of ME dynamics with thickness. The inset of (f) shows the normalization basis of Amp$_{575}$.

rapidly decays, and (ii) a PIA band with a decay constant of 15 ps forms near 600 nm (see Fig. S9 for the time-resolved transient spectra and fitting details). The spectrally narrow and long-lived component of the dominant PIB peak, which is consistently observed under all conditions, is attributed to the recovery of the ground state from single exciton (SE) excitation, indicating its origin from initial population depletion.

To quantify these excitation-dependent dynamics, we normalized the transient spectral responses to the amplitude of the longest-lived decay component of the PIB band (see the inset of Fig. 2f). The normalized kinetics clearly reveals the emergence of a 15 ps decay component under intense excitation, as verified by multi-exponential fitting (see Fig. S10). The 15 ps component appears at both the 575 nm (PIA) and 750 nm (PIB) regions. To quantify this component, we extracted its amplitude (Amp_{575}) from nonlinear least-squares fitting, as shown in Fig. 2e. Amp_{575} represents the population of the ME state and increases super-linearly with pump fluence (see Fig. S11). Fig. 2f shows the normalized amplitude (Amp_{575}/Amp_{750}), using the long-lived PIB band at 750 nm as a reference. This ratio decreases with increasing film thickness, indicating that ME-related dynamics are gradually suppressed in thicker films. Notably, ME-associated dynamics and other excited-state processes in perovskite films are known to exhibit significant thickness dependence.[48,49] The observed fast decay (~15 ps) reflects the instantaneous depopulation dynamics of the ME state rather than the ASE pulse duration itself. We note that while the temporal evolution of the ME state and the ASE time profile may show correlation, they represent distinct physical quantities. To directly observe the temporal dynamics of ASE, ultrafast time-resolved photoluminescence techniques such as fluorescence up-conversion would be required.

In a conventional four-level laser system, the initially excited state rapidly undergoes nonradiative relaxation to a lower-lying state with strong oscillator strength, where population inversion can be achieved for stimulated emission. However, in hybrid perovskite films, it is well known that excitons generated by photoexcitation undergo ultrafast charge separation, typically within hundreds of femtoseconds.[50,51] This suggests that the lifetime of the population-inverted state may not be sufficient for ASE operation. Although population inversion might be formally possible between the charge-separated (CS) state and an intermediate state near the band-edge state, this scenario is unlikely, given the proximity of the observed ASE band to the bandgap energy. Although free carriers are indeed generated almost instantaneously after photoexcitation, their direct recombination to the ground state is forbidden and thus contributes negligibly to ASE. As a result, the longer-lived ME states are far more likely to serve as the upper level for the observed optical gain, consistent with the dynamics discussed in this study.

The 15 ps component appearing only under high excitation fluence is strongly correlated with ASE, and thus likely represents an electronic state involved in the optical gain dynamics. As shown in Fig. 2 and S7, the 15 ps component and PIA in the short-wavelength region (relative to the

bandgap) exhibit a strong pump fluence dependence. Such intensity-dependent spectral evolution provides clear evidence for ME formation, which is a general characteristic of semiconductor materials described in detail in a recent publication.[54] Based on the fluence dependence and spectral features, it is highly possible that the 15 ps component is attributed to an ME state. Consistent with this, previous studies have similarly assigned short-wavelength PIA features to multiexcitonic contributions.[46,49] While it is conceivable that hot-state absorption, in principle, contributes to the observed PIA, such processes involve exciton-to-vibrational or higher-lying exciton transitions. These transitions, although possible without multiphoton excitation, are statistically less probable than the exciton–exciton interactions responsible for ME formation at high excitation densities. This further supports our assignment of the 15 ps PIA feature to ME dynamics rather than hot-carrier effects. The singly excited exciton and ME states are transition-allowed states, so that the transitions between the SE and ME states may participate in the ASE process.

Under intense photoexcitation, both SE and ME states are populated, as schematically illustrated in Fig. 3a. The SE state rapidly relaxes to the CS state within hundreds of femtoseconds, whereas the ME state persists for approximately 15 ps. This lifetime mismatch – rapid depletion of the lower SE level *versus* slow decay of the upper ME level – results in a transient population inversion (Fig. 3b). Radiative relaxation from the ME state to the SE state creates photons, as shown in Fig. 3c. These emitted photons induce multiple stimulated emission processes involving the transition between the ME and SE states, leading to ASE. Fig. 3d shows the stimulated emission process from the ME to SE transition that leads to ASE. The transition energy between the ME and SE states is expected to lie slightly below the bandgap energy, which agrees well with the position of the observed ASE band.

The population of the ME state decreases monotonically with increasing film thickness (Fig. 2e). However, this trend alone cannot account for the non-monotonic behavior of the ASE threshold, particularly the initial reduction at thinner film thicknesses (Fig. 1g). In a perovskite film, photons emitted *via* stimulated emission from the ME state may be partially confined within the film due to internal reflections, analogous to an optical cavity. Fig. 4a presents the spatial profile of the static electric field of 790 nm light within MAPbI$_3$ films of varying thicknesses (50 nm, 200 nm, and 400 nm), calculated at 790 nm – the peak wavelength of the ASE spectrum. Increasing the film thickness relatively broadens the region over which the electric field is localized within the film. Considering that optical excitation occurs either from the top of the perovskite or through the substrate, the spatial overlap between the exponentially decaying pump intensity and the electric field distribution can vary with the film thickness. When the film thickness is much thinner than the effective absorption length (~75 nm), the integrated field amplitude inside the film remains low, indicating the difficulty of confining photons. As the film thickness increases, the confinement factor also increases (Fig. 4b). However, distinct dips are
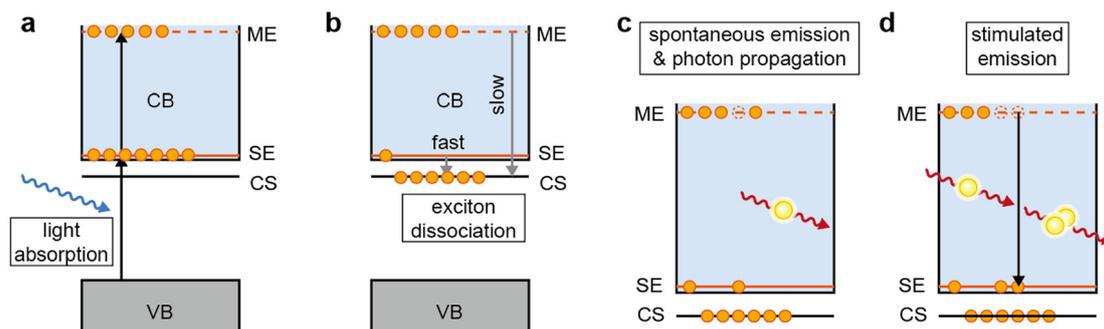
Fig. 3 Schematic illustration of the exciton dynamics and ASE mechanism in the MAPbI₃ films. (a) Light absorption and ME formation. (b) Exciton dissociation into SE and the charge separation of the SE state. (c) Spontaneous emission and photon propagation. (d) Stimulated emission involving the ME and SE states under population inversion.
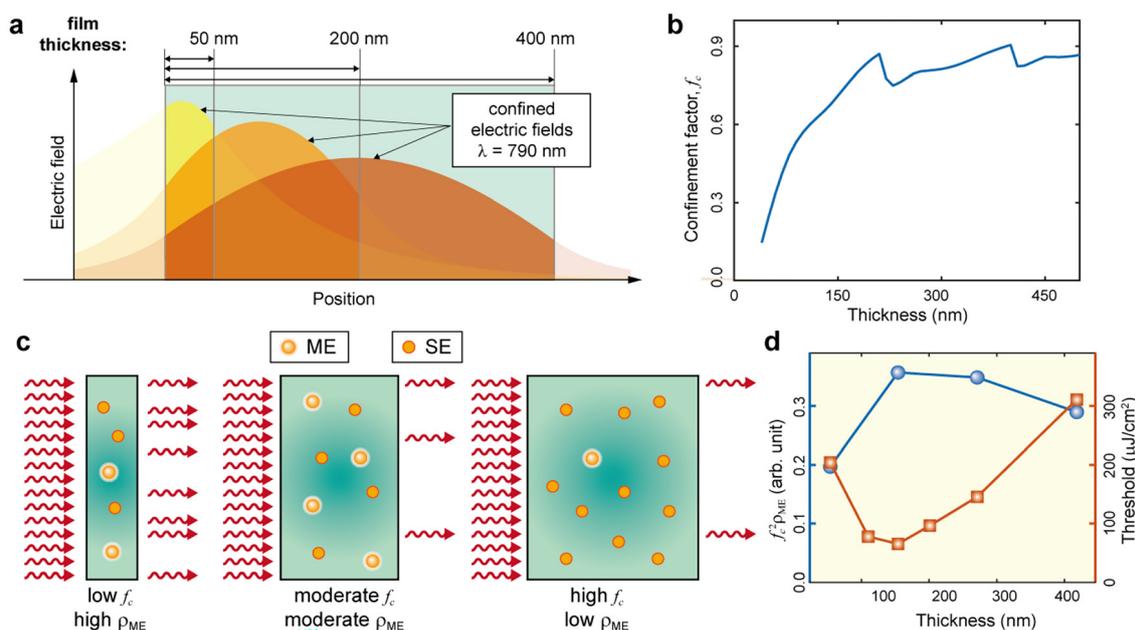

Fig. 4 (a) Electric field profiles obtained from perovskite films of different thicknesses (50, 200, and 400 nm). (b) Thickness dependence of the optical confinement factor. (c) Schematic illustration of the thickness-dependent ASE mechanism of perovskites films. (d) ASE efficiency (blue) estimated by considering f_c and ρ_{ME}. The ASE threshold fluence (red) is overlaid for comparison.

observed near 200 nm and 400 nm. These reductions correspond to the onset of higher-order TE modes, as shown in Fig. 1c. The confinement factor Γ_m of the m-th guided mode in the perovskite film is defined as follows:

$$\Gamma_m = \frac{\int_{\text{perovskite}} |E_m(x)|^2 dx}{\int_{\text{all layers}} |E_m(x)|^2 dx}$$

where $E_m(x)$ is the electric field profile of mth order and x denotes the position perpendicular to the film surface. The coupling weight P_m of each guide mode represents the fraction of the input field that couples into that mode and is calculated as follows:

$$P_m = \frac{\left|\int E_{\text{in}}(x) \cdot E_m^*(x) dx\right|^2}{\sum_n \left|\int E_{\text{in}}(x) \cdot E_n^*(x) dx\right|^2}$$

where $E_{\text{in}}(x)$ is the incident electric field. It can be modeled as an exponential function according to Beer–Lambert's law, reflecting the absorption of photons as the electric field propagates through the perovskite film. In our analysis, the total confinement factor, f_c, is calculated as $f_c = \Sigma_m \Gamma_m P_m$. For film thicknesses around 200 nm, the effective refractive index of the TE₁ mode (approximately 1.42) becomes substantially lower than those of the TE₀ and TM₀ modes (approximately 2.25 and 2.05, respectively). As a result, when all supported

modes are included, the total confinement factor does not necessarily increase monotonically with thickness. Thus, the emergence of additional guided modes leads to mode competition, thereby reducing the coupling strength of the previously dominant TE_0 mode, which manifests as dips in the total confinement factor, f_c. The confinement factors and coupling weights of the individual guided modes, including higher-order modes, as a function of film thickness, are shown in Fig. S12a and S12b, respectively.

Fig. 4c shows the thickness-dependent behavior of ASE efficiency, governed by the optical confinement factor f_c and the ME density (ρ_{ME}). In thinner films, the number of particles interacting with the pump pulse is smaller due to the reduced volume. Consequently, there is a higher probability for a single particle to undergo multiple light–matter interactions, which facilitates the formation of ME states. It should be noted that perovskites are not low-density molecular systems, and thus multiphoton effects can readily occur under high photon flux conditions. However, the poor optical confinement in these films prevents efficient stimulated emission, demonstrating that a high ME population alone is insufficient to induce ASE. Conversely, as the film thickness increases, f_c improves, but ρ_{ME} decreases because the carrier density is diluted over a large volume, favoring the formation of the SE state. Consequently, optimal ASE performance is achieved only when both ρ_{ME} and f_c reach sufficient levels simultaneously. For $MAPbI_3$, this balance occurs at around 150 nm, consistent with our experimental results.

To quantitatively estimate ASE efficiency, we considered the product of the relative ME population (obtained from PP measurements) and the square of the optical confinement factor, as shown in Fig. 4d. The confinement factor is squared to reflect the intensity dependence, since experimental measurements are typically intensity-based rather than field-based. The resulting curve, representing the effective ASE efficiency, peaks near 100 nm and subsequently decreases, showing excellent agreement with the experimental trend of the ASE threshold plotted for comparison. This agreement confirms that the interplay between the ME population and optical confinement is indeed the causal mechanism governing the thickness-dependent ASE performance. One important caveat, however, is that this study assumes the ME state to be primarily a biexciton. In thinner films, the probability of forming higher-order exciton states may not be negligible. Under lasing operational conditions, the formation of such higher-order excitons is even more likely. Therefore, for future extension toward laser device applications, a more quantitative investigation of multiexciton dynamics will be essential.

Conclusions

In summary, this study reveals how the thickness of $MAPbI_3$ perovskite films influences the ASE threshold. We attribute the non-monotonic dependence of the ASE threshold on film thickness to two distinct factors: ME-state population and

optical confinement. Pump–probe measurements show that ME-state formation, which contributes to population inversion, is favored in thinner films, whereas thicker films suppress this process despite offering improved optical confinement. Slab-waveguide analysis[52] confirms that optical confinement improves with increasing film thickness, but becomes ineffective in very thick films due to insufficient field overlap. Based on the experimentally extracted ME population and the calculated optical confinement – taking into account the spatial overlap between the incident excitation profile and the optical-field distribution within the perovskite film layer – we estimate that the ASE threshold reaches a minimum at a film thickness near 150 nm. This estimation was experimentally validated, with the lowest ASE threshold observed at a film thickness of 154 nm. These results provide important design principles for further lowering the ASE and lasing thresholds under continuous-wave operation at room temperature, as well as in electrically driven laser diodes.

Methods

Film preparation

Methylammonium iodide (MAI) and lead iodide (PbI_2) were purchased from Greatcell Solar and Sigma-Aldrich, respectively. Dimethylformamide (DMF) and toluene were also obtained from Sigma-Aldrich. All chemicals were used without further purification. Precursor solutions were prepared by dissolving MAI and PbI_2 in DMF at concentrations ranging from 0.2 M to 1.2 M. Glass substrates were sequentially cleaned in air using soapy water, deionized water, acetone, and isopropyl alcohol, followed by 20 minutes of UV–ozone treatment prior to film deposition. The perovskite films were spin-coated at 4000 rpm, and a solvent-quenching step was performed by dispensing 120 μL of toluene onto the spinning substrate after 5 s. The samples were then annealed at 70 °C for 5 minutes.

ASE characterization

ASE experiments were performed using a pulsed-laser source (PNP-M08010-130, Teem Photonics), which delivers the second harmonic of a neodymium-doped yttrium aluminum garnet (Nd:YAG) laser with a pulse duration of 400 ps and a repetition rate of 1 kHz. Emission spectra were obtained at room temperature using a fiber-coupled spectrograph (Kymera 328i-A) equipped with a thermoelectrically cooled silicon CCD detector (DV420A-OE, Andor Technology).

Slab-waveguide analysis

Calculations of the guided modes, effective refractive indices, and optical confinement factors for the slab-waveguide structure were performed using the online tool 1-D Mode Solver for Dielectric Multilayer Slab Waveguides.[52] The thickness and refractive index values of the $MAPbI_3$ perovskite layer were adopted from a previously reported study.[42]

Femtosecond PP spectroscopy

The pump pulse (480 nm) was generated by second-harmonic generation of a near-infrared pulse produced by a home-built noncollinear optical parametric amplifier, where the fundamental light source is a Yb optical amplifier (Pharos, Light Conversion) with a pulse energy of 1.5 μJ and a repetition frequency of 100 kHz.[53] The NOPA used in this study provided a tunable output in the range of 650–960 nm, along with its second harmonics. Among the available wavelengths, 480 nm was selected as the pump for the pump–probe measurements, as it was the closest accessible wavelength to the 532 nm excitation used in the ASE experiments. A small portion of the fundamental beam was separated to generate a supercontinuum probe through the self-phase phenomenon at a YAG crystal. The pulse energy of the probe was reduced by less than 100 pJ to minimize the contribution of probe–matter interaction in the time-resolved spectra. An optical chopper was installed at the pump line for frequency modulation. The modulation frequency was 1 kHz, where it is synchronized to the readout rate (2 kHz) of the spectrometer. To distinguish the spectra obtained with the pump beam on and off, we simultaneously recorded a digital signal indicating the pump status along with the probe spectrum. For each time delay, 500 probe spectra were acquired, consisting of 250 with the pump on and 250 with the pump off. The final signal was obtained by subtracting the averaged pump-off spectra from the averaged pump-on spectra.

Conflicts of interest

There are no conflicts to declare.

Data availability

The authors confirm that the data supporting the findings of this study are available within the article and its supplementary information (SI), and more data can be made available from the corresponding author upon request.

Supplementary information: ASE spectra with polar plots of peak ASE intensity for both thin and thick perovskite films, XRD patterns for films of various thicknesses, femtosecond pump–probe spectra obtained from four different film thicknesses under four distinct pump fluences, time profiles at 575 nm and 750 nm extracted from the original pump–probe spectral data, and the optical confinement factor with coupling weight for all guided modes in the perovskite film. See DOI: https://doi.org/10.1039/d5nr03886c.

Acknowledgements

References

1 N. Li, *et al.*, Integrated lasers on silicon at communication wavelength: a progress review, *Adv. Opt. Mater.*, 2022, **10**, 2201008.

2 E. Pelucchi, *et al.*, The potential and global outlook of integrated photonics for quantum technologies, *Nat. Rev. Phys.*, 2022, **4**, 194–208.

3 M. F. Spencer, *et al.*, Applications of Lasers for Sensing and Free Space Communications: introduction to the feature issue, *Appl. Opt.*, 2023, **62**, ALS1–ALS4.

4 H. Dong, *et al.*, Metal Halide Perovskite for next-generation optoelectronics: progresses and prospects, *ELight*, 2023, **3**, 3.

5 H. Tang, Z. Jia, Y. Xu, Y. Liu and Q. Lin, Enhanced photoluminescence quantum yield of metal halide perovskite microcrystals for multiple optoelectronic applications, *Small*, 2024, **20**, 2304336.

6 Z. Zang, S. Zhao, W. Cai and H. Wang, *Inorganic Perovskite Materials and Devices*, Springer, 2024, pp. 139–170.

7 S. Chen, *et al.*, A photonic crystal laser from solution based organo-lead iodide perovskite thin films, *ACS Nano*, 2016, **10**, 3959–3967.

8 C.-Y. Huang, *et al.*, $CsPbBr_3$ perovskite quantum dot vertical cavity lasers with low threshold and high stability, *ACS Photonics*, 2017, **4**, 2281–2289.

9 K. Roh, *et al.*, Widely tunable, room temperature, single-mode lasing operation from mixed-halide perovskite thin films, *ACS Photonics*, 2019, **6**, 3331–3337.

10 T. Liang, W. Liu, X. Liu, Y. Li and J. Fan, Fabry–Perot Mode-Limited High-Purcell-Enhanced Spontaneous Emission from In Situ Laser-Induced $CsPbBr_3$ Quantum Dots in CsPb2Br5 Microcavities, *Nano Lett.*, 2021, **22**, 355–365.

11 P. Brenner, *et al.*, Continuous wave amplified spontaneous emission in phase-stable lead halide perovskites, *Nat. Commun.*, 2019, **10**, 988.

12 Y. Jia, R. A. Kerner, A. J. Grede, B. P. Rand and N. C. Giebink, Continuous-wave lasing in an organic–inorganic lead halide perovskite semiconductor, *Nat. Photonics*, 2017, **11**, 784–788.

13 C. Qin, *et al.*, Stable room-temperature continuous-wave lasing in quasi-2D perovskite films, *Nature*, 2020, **585**, 53–57.

14 X. Li, *et al.*, Stable whispering gallery mode lasing from solution–processed formamidinium lead bromide perovskite microdisks, *Adv. Opt. Mater.*, 2020, **8**, 2000030.

15 W. B. Gunnarsson, *et al.*, Toward nonepitaxial laser diodes, *Chem. Rev.*, 2023, **123**, 7548–7584.

16 I. Goldberg, *et al.*, Toward Thin–Film Laser Diodes with Metal Halide Perovskites, *Adv. Mater.*, 2024, **36**, 2314193.

17 X. Wang, *et al.*, Quasi-2D Dion-Jacobson phase perovskites as a promising material platform for stable and high-performance lasers, *Sci. Adv.*, 2023, **9**, eadj3476.

18 Y. Zhang, *et al.*, Enhanced performance of amplified spontaneous emission in Dion-Jacobson phase quasi-2D perovskite by facilitating carrier co-radiation, *Opt. Express*, 2024, **32**, 26306–26317.

19 K. K. Bhowmik, *et al.*, Enhanced Amplified Spontaneous Emission from Optically Pumped Perovskite Light–Emitting Diodes with Sodium Fluoride Additives, *Adv. Photonics Res.*, 2025, 2500025.

20 Y. Tang, *et al.*, Amplified spontaneous emission from waveguides based on hybrid quasi-2D perovskites of Dion–Jacobson and Ruddlesden–Popper phases, *J. Mater. Chem. C*, 2023, **11**, 10043–10050.

21 M. Anni, A. Perulli and G. Monti, Thickness dependence of the amplified spontaneous emission threshold and operational stability in poly (9, 9-dioctylfluorene) active waveguides, *J. Appl. Phys.*, 2012, **111**, 093109.

22 E. M. Calzado, M. G. Ramírez, P. G. Boj and M. A. D. García, Thickness dependence of amplified spontaneous emission in low-absorbing organic waveguides, *Appl. Opt.*, 2012, **51**, 3287–3293.

23 Y. Mao, *et al.*, Enhancing Amplified Spontaneous Emission in Perovskite Thin Films by Thickness Regulation: Insights into Carrier Distribution and Optical Confinement, *Adv. Opt. Mater.*, 2025, 2500307.

24 S. M. Qaid, M. N. Khan, A. Alqasem, M. Hezam and A. Aldwayyan, Restraining effect of film thickness on the behaviour of amplified spontaneous emission from methylammonium lead iodide perovskite, *IET Optoelectron.*, 2019, **13**, 2–6.

25 N. Annavarapu, *et al.*, Four–Dimensional Design Space of High–Q Second–Order Distributed Feedback Perovskite Lasers, *Adv. Opt. Mater.*, 2024, **12**, 2302496.

26 R. F. Moral, *et al.*, Influence of the vibrational modes from the organic moieties in 2D lead halides on excitonic recombination and phase transition, *Adv. Opt. Mater.*, 2020, **8**, 2001431.

27 J. Qin, *et al.*, From optical pumping to electrical pumping: the threshold overestimation in metal halide perovskites, *Mater. Horiz.*, 2023, **10**, 1446–1453.

28 J. Zhang, *et al.*, Transport layer engineering toward lower threshold for perovskite lasers, *Adv. Mater.*, 2023, **35**, 2300922.

29 C. Zuo, *et al.*, Advances in perovskite solar cells, *Adv. Sci.*, 2016, **3**, 1500324.

30 S. D. Stranks, *et al.*, Electron-hole diffusion lengths exceeding 1 micrometer in an organometal trihalide perovskite absorber, *Science*, 2013, **342**, 341–344.

31 Z. Liu, *et al.*, Gas-solid reaction based over one-micrometer thick stable perovskite films for efficient solar cells and modules, *Nat. Commun.*, 2018, **9**, 3880.

32 Q. Wan, *et al.*, Ultrathin light-emitting diodes with external efficiency over 26% based on resurfaced perovskite nanocrystals, *ACS Energy Lett.*, 2023, **8**, 927–934.

33 Z. Xiao, *et al.*, Efficient perovskite light-emitting diodes featuring nanometre-sized crystallites, *Nat. Photonics*, 2017, **11**, 108–115.

34 L. Zhao, K. M. Lee, K. Roh, S. U. Z. Khan and B. P. Rand, Improved outcoupling efficiency and stability of perovskite light–emitting diodes using thin emitting layers, *Adv. Mater.*, 2019, **31**, 1805836.

35 X. Huang, *et al.*, Improved performance of perovskite light-emitting diodes with a NaCl doped PEDOT: PSS hole transport layer, *J. Mater. Chem. C*, 2021, **9**, 4344–4350.

36 S. D. Baek, *et al.*, Exciton Dynamics in Layered Halide Perovskite Light–Emitting Diodes, *Adv. Mater.*, 2024, 2411998.

37 D. Zhang, *et al.*, Suppressing thermal quenching via defect passivation for efficient quasi-2D perovskite light-emitting diodes, *Light: Sci. Appl.*, 2022, **11**, 69.

38 L. Zhao, *et al.*, Thermal management enables bright and stable perovskite light–emitting diodes, *Adv. Mater.*, 2020, **32**, 2000752.

39 L. Zhao, *et al.*, Nanosecond–pulsed perovskite light–emitting diodes at high current density, *Adv. Mater.*, 2021, **33**, 2104867.

40 Y.-J. Jung, S.-Y. Cho, J.-W. Jung, S.-Y. Kim and J.-H. Lee, Influence of indium-tin-oxide and emitting-layer thicknesses on light outcoupling of perovskite light-emitting diodes, *Nano Convergence*, 2019, **6**, 1–5.

41 Y.-S. Park, J. Roh, B. T. Diroll, R. D. Schaller and V. I. Klimov, Colloidal quantum dot lasers, *Nat. Rev. Mater.*, 2021, **6**, 382–401.

42 G. Lee, B. P. Rand and K. Roh, Halide Perovskite Thin Film Lasing Mode Control, *ACS Appl. Mater. Interfaces*, 2024, **16**, 55650–55657.

43 Y.-H. Hong and T. S. Kao, Room-temperature random lasing of metal-halide perovskites via morphology-controlled synthesis, *Nanoscale Adv.*, 2020, **2**, 5833–5840.

44 T. C. Sum, *et al.*, Spectral features and charge dynamics of lead halide perovskites: origins and interpretations, *Acc. Chem. Res.*, 2016, **49**, 294–302.

45 S. Biswas, J. Kim, X. Zhang and G. D. Scholes, Coherent Two-Dimensional and Broadband Electronic Spectroscopies, *Chem. Rev.*, 2022, **122**, 4257–4321, DOI: 10.1021/acs.chemrev.1c00623.

46 X. Deng, *et al.*, Ultrafast carrier dynamics in methylammonium lead bromide perovskite, *J. Phys. Chem. C*, 2016, **120**, 2542–2547.

47 D. M. Niedzwiedzki, H. Zhou and P. Biswas, Exciton binding energy of MAPbI3 thin film elucidated via analysis and modeling of perovskite absorption and photoluminescence properties using various methodologies, *J. Phys. Chem. C*, 2022, **126**, 1046–1054.

48 M. Gramlich, *et al.*, Thickness-dependence of exciton–exciton annihilation in halide perovskite nanoplatelets, *J. Phys. Chem. Lett.*, 2020, **11**, 5361–5366.

49 Y. Liu, *et al.*, Efficiency of MAPbI3-based planar solar cell analyzed by its thickness-dependent exciton formation, morphology, and crystallinity, *ACS Appl. Mater. Interfaces*, 2019, **11**, 14810–14820.

50 I. Minda, J. Horn, E. Ahmed, D. Schlettwein and H. Schwoerer, Ultrafast charge dynamics in mixed cation–mixed halide perovskite thin films, *ChemPhysChem*, 2018, **19**, 3010–3017.

51 B. Guzelturk, *et al.*, Terahertz emission from hybrid perovskites driven by ultrafast charge separation and strong electron–phonon coupling, *Adv. Mater.*, 2018, **30**, 1704737.

52 Q. Sun, B. Dereka, E. Vauthey, L. M. L. Daku and A. Hauser, Ultrafast transient IR spectroscopy and DFT cal-culations of ruthenium(II) polypyridyl complexes, *Chem. Sci.*, 2017, **8**, 223–230, DOI: 10.1039/C6SC01220E.

53 J. Kim, H. S. Lee and C. H. Kim, Observation of Coherent Symmetry-Breaking Vibration by Polarization-Dependent Femtosecond Spectroscopy, *J. Phys. Chem. B*, 2024, **128**, 1053–1060, DOI: 10.1021/acs.jpcb.3c08151.

54 P. Malý, *et al.*, Separating single- from multi-particle dynamics in nonlinear spectroscopy, *Nature*, 2023, **616**, 280–287, DOI: 10.1038/s41586-023-05846-7.